

# Massive MIMO Channel Measurements and Achievable Rates in a Residential Area

Marc Gauger\*, Maximilian Arnold\* and Stephan ten Brink\*

\*Institute of Telecommunications, Pfaffenwaldring 47, University of Stuttgart, 70569 Stuttgart, Germany

**Abstract**—In this paper we present a measurement set-up for massive MIMO channel sounding that shows very good long-term phase stability. Initial measurements were performed in a residential area to evaluate different conventional precoding schemes such as maximum ratio transmission and phase only precoding. A massive amount of data points was collected, with 924 times 64 complex channel weights per data point. Each data point is position-tagged using differential GPS with real-time kinematik, achieving better than 35cm position accuracy in more than 90% of the collected data points, making this dataset a rich resource for, e.g., further studying machine learning based, data-driven approaches in wireless communications.

## I. INTRODUCTION

Massive multiple-input multiple-output (MIMO) is a key enabling technology for the future wireless “5G” standard and beyond [1]–[3]. To evaluate massive MIMO algorithms and achievable sum-rate capacities, several channel models have been established in the literature [4], [5]. However, channel models can only provide an abstract view considering the most important wireless propagation phenomena, and do often model specific communication scenarios and hardware impairments only rudimentarily. Thus, actual channel measurements in typical coverage settings, like performed in this paper, offer the potential of providing much more realistic estimates on the actual achievable data rates and their particular distribution over the spatial coverage region.

## II. MEASUREMENT SET-UP

The objective of this measurement campaign is to obtain actual measured channel data (i.e., CSI, channel state information) of a typical residential massive multiple input, multiple output (MIMO) antenna set-up. For studying the effects of multiuser operation, position-labeled single-input/single output (SIMO) measurements are required. Conceptually, the measurements could be performed using two possible set-ups when assuming channel reciprocity: (1) multiple transmit antennas at the basestation, and one antenna at the mobile receiver, or, (2) multiple receive antennas at the basestation, and one antenna at the mobile transmitter. Option (1) requires a potentially large number of orthogonal pilots and perfect frequency and time-alignment of the multiple transmitters, but simplifies receiver post-processing; option (2) simplifies pilot design but requires much more involved post-processing of the multiple received signals. We opted for set-up (2) as receiver imperfections, e.g., carrier frequency offset (CFO), can be more conveniently compensated on a per-antenna basis via post-processing; also, the mobile transmitter having only a single antenna is easier to implement and more lightweight to carry around.

### A. Portable Transmitter

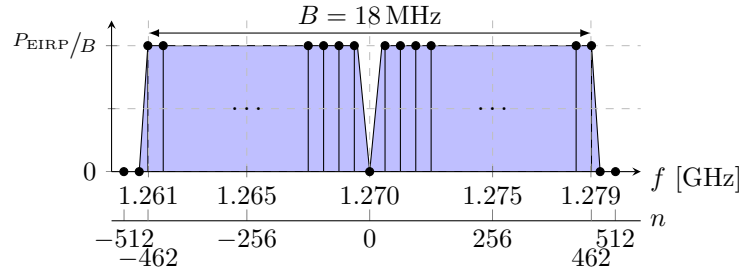


Fig. 1: Spectrum of transmitted OFDM signal and corresponding subcarrier index  $n$

The transmitter is based on an Ettus USRP B210 [6]. Its Field Programmable Gate Array (FPGA) was programmed to generate orthogonal frequency-division multiplexing (OFDM) symbols of  $B = 18$  MHz effective bandwidth. An OFDM sample rate of  $R_s = \frac{1}{T_s} = 20$  MS/s and a number of  $N_{\text{sub}} = 1024$  subcarriers are used. The subcarrier spacing is about  $\Delta f_{\text{sub}} = \frac{R_s}{N_{\text{sub}}} \approx 20$  kHz. At either band edge, 49–50 subcarriers were set to zero to relax the requirements for analog filtering; also, the direct current (DC) subcarrier was set to zero for carrier leakage reduction; thus, in total 924 subcarriers are effectively used, as depicted in Fig. 1. The carrier frequency was set to the unlicensed ham radio frequency 1.27 GHz so that a rather large transmit peak envelope power (PEP) of 18 W ( $P_{\text{TX}} = 42$  dBm) in combination with a dipole antenna could be used. In this frequency range a PEP of up to 750 W is allowed for licensed ham radio. The transmitter dipole antenna has a gain of about  $G_{\text{TX}} = 9$  dBi and is vertically polarized, yielding an effective (or equivalent) isotropic radiated power (EIRP) of about 51 dBm.

Fig. 3 shows the link budget for a line-of-sight (LOS) channel.  $G_{\text{RX}}$  is the receiver (RX) antenna gain. The total measurement time was 8 hours, where the compact hand-wagon was manually pushed around in a residential area of size about 600 m  $\times$  800 m (Fig. 2).

1) *GPS positioning*: The position of the wagon was determined by the Global Positioning System - Real Time Kinematic (GPS-RTK) using RTKLIB [7]. The hardware used is based on two “ublox” NEO-M8T GPS receivers, with a dedicated GPS basestation fixed at the roof-top of the Institute of Telecommunications, University of Stuttgart. For illustration, Fig. 4 shows the horizontal standard deviations with respect to North, East and the vertical standard deviation with respect to “Upper” of the GPS positioning of the RTKLIB. As can be



Fig. 2: Map of considered residential area of dimension  $600\text{ m} \times 800\text{ m}$ ; basestation location marked with a red “X”

seen (magenta lines in Fig. 4) the  $(x, y)$  –accuracy was better than 34 cm in more than 90% of the measurement points (with a 5 Hz update rate).

2) *OFDM frame structure*: The OFDM symbols are composed of 924 subcarriers. The symbol duration with cyclic prefix is  $T_{\text{OFDM}} = (N_{\text{sub}} - N_{\text{CP}}) \cdot T_s = (1024 + 256) \cdot \frac{1}{20\text{ MS/s}} = 64\ \mu\text{s}$ , where 25% (i.e.,  $N_{\text{CP}} \cdot T_s = 256 \cdot \frac{1}{20\text{ MS/s}} = 12.8\ \mu\text{s}$ ) of the symbol duration was used as cyclic prefix (CP). One frame is built of two pilot OFDM symbols and one data OFDM symbol. The frames are repeated without any pause or null symbol. The two pilot OFDM symbols are used for channel sounding and CFO estimation. The data OFDM symbol is binary phase shift keying (BPSK) modulated and contains an ID corresponding to the actual GPS position. The bandwidth can be chosen freely, yet needs to stay smaller than 56 MHz due to the limitations of the USRP [6]. For the channel measurements in this paper, we used an 18 MHz OFDM signal bandwidth with sampling rate  $\frac{1}{T_s} = 20\text{ MS/s}$  at a carrier frequency of 1.27 GHz.

### B. Massive MIMO Receiver

The receiver uses a 64-element antenna array with dual polarized patch antennas, while only the vertical polarization was used. The 64 full radio frequency (RF) chains are implemented in a multi-board/daughter-board configuration to filter, amplify and downconvert (i.e., frequency shift) the respective antenna signals. The 64 antenna signals of 18 MHz bandwidth, all centered around the carrier frequency of 1.27 GHz, are shifted

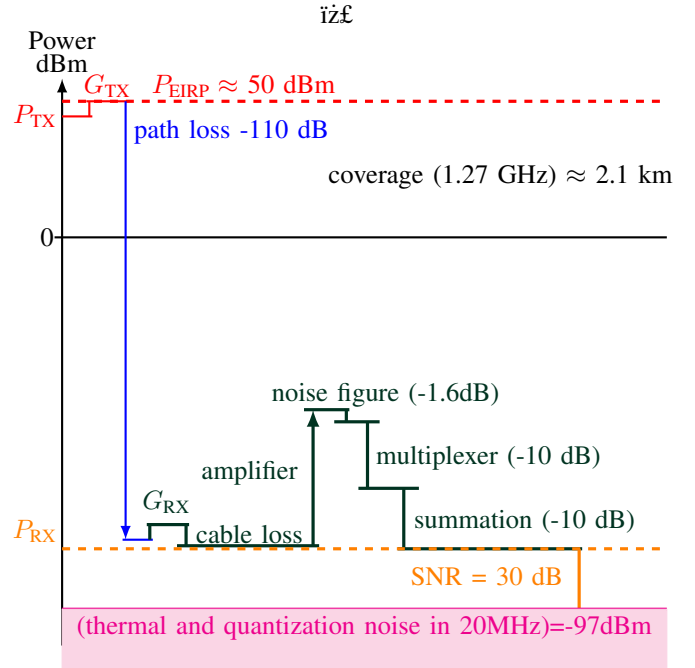


Fig. 3: Overview of link budget from TX to RX, resulting in an expected coverage radius of about 2.1km

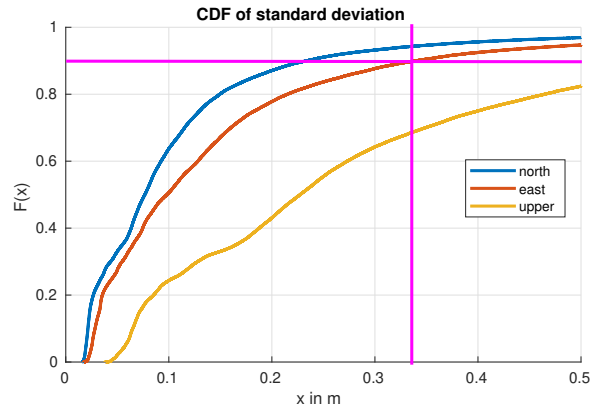


Fig. 4: CDF of standard deviation of GPS position accuracy estimated by RTKLIB [7]

to different intermediate frequencies by means of separately programmable downconverters so that the individual spectra do not overlap in a spectral band from 10 MHz to 2 GHz. This composite “frequency division multiple antenna”-signal is then analog-to-digital converted and stored on a Solid-State-Drive (SSD) drive by a digital oscilloscope Teledyne LeCroy WavePro 604HD, allowing to measure spatial snapshots of 64 antennas times 924 subcarriers complex channel state information (CSI) samples at a rate of  $\sim 11$  measurements points per second (comp. [8] for more details).

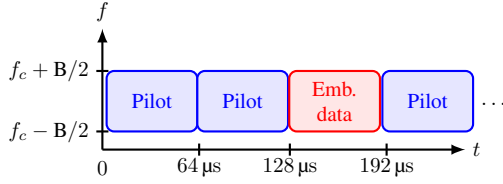


Fig. 5: Transmitted OFDM time-domain signal with pilot symbols and data symbols carrying GPS data



Fig. 6: Photos of basestation receiver antenna with 64 antenna elements

### C. Extraction of Channel State Information

All 64 antenna signals are perfectly time synchronized in the digital domain by jointly digitizing the composite “frequency division multiple antenna”-signal using the single analog to digital converter (A/D converter) of the digital scope (in fact, four A/D converters of the scope were used which, however, are perfectly synchronized). The repeated two pilots symbols are used for the frame detection, channel estimation and for CFO estimation by employing

$$\Delta f_{\text{CFO}} = \frac{1}{2\pi N_{\text{sub}} T_s} \sum_{\ell=0}^{N_{\text{sub}}-1} y(t_0 + \ell) \cdot y(t_0 + N_{\text{sub}} + N_{\text{CP}} + \ell)^* \quad (1)$$

To obtain a measurement set-up which is stable over several hours, all CSI phases are calibrated to a reference transmitter which was at a fixed position only a few meters away from the antenna array. The (narrowband) reference transmitter was set to a carrier frequency of 1.257 GHz with a spectral bandwidth of 1.5 MHz. This way, any phase jitter/phase flips etc. of the RF chains that may occur due to the individual phase locked loop (PLL) control loops are implicitly accounted for. Also, to account for different gains of the RF chains, the power of the individual signals is further calibrated by estimating the signal-to-noise ratio (SNR) per RF-chain, and aligning the noise floor across all antenna signals by respective amplitude scaling. To further reduce the noise, i.e., to improve the SNR, the time-domain channel impulse response was computed from the frequency domain channel estimates CSI, and cut off so that multipath delays up to 0.82 ms corresponding to a maximal path difference of 1.92 km were accounted for

(i.e., 128 samples at  $T_s = \frac{1}{20} \mu\text{s}$ ). The RX antenna array was located at position  $(x, y) = (0\text{m}, 0\text{m})$  on a roof-top height of 40 m above ground and is marked in the figures with a red cross (“X”). The RX antenna array was facing toward the South-East.

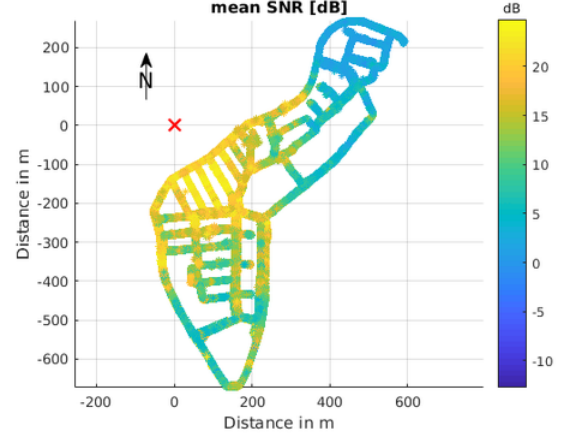


Fig. 7: Plot of mean SNR over coverage area; basestation array antenna at  $(x, y) = (0\text{m}, 0\text{m})$ , 40m height, facing South-East

Fig. 7 plots the mean SNR computed across all 64 RX antennas. As expected, the area in the North has to have a smaller SNR due to the limited half power beam width of  $69.1^\circ$  of the receiver array’s patch antennas.

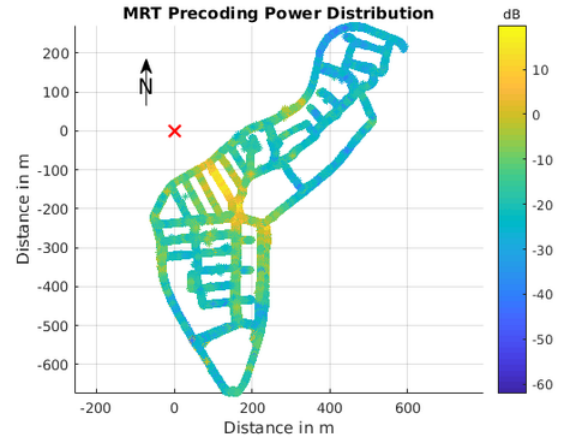


Fig. 8: Illustration of the effect of MRT precoding to a point at  $(x, y) = (110\text{m}, -120\text{m})$

As one sanity check for the measured data, Fig. 8 illustrates the distribution of the signal power if MRT precoding is applied to a position at  $(110\text{m}, -120\text{m})$ , resulting in a quite plausible beam/focus area around the desired “target” user point in comparison to the “mean-SNR” shown in Fig. 7 .

### III. K-MEANS CLUSTERING: PHASE ONLY VS MRT

One way of evaluating the achievable sum-rate of this residential area setting is to apply a  $k$ -means clustering algorithm, to find areas that are “quasi” mutually orthogonal

to each other, i.e., the vector product  $\langle X, Y \rangle$  is very small, with  $X$  taken from cluster  $i$ , and  $Y$  taken from cluster  $j$ , with  $2 \leq i, j \leq K$ . An overview of clustering schemes in massive MIMO can be found in [9].

### A. Precoding and Clustering Algorithm

Next, we outline the details of the clustering algorithm for the two precoding techniques MRT and Phase Only (PO), respectively. Algorithm 1 describes a  $k$ -means clustering with an MRT precoding weight function, and Algorithm 2 describes the version using a PO weight function.

---

#### Algorithm 1 $k$ -means MRT Algorithm

---

- 1:  $M$  number of measurements
  - 2:  $k = 1, \dots, K; \mathbf{C} \in \mathbb{C}(N_{\text{antennas}} \times K) = \mathbf{c}_1, \dots, \mathbf{c}_K$
  - 3:  $\mathbf{H} \in \mathbb{C}(M \times N_{\text{antennas}})$
  - 4: Randomly choose  $K$  different indices of measurements
  - 5: Define center of cluster as  $\mathbf{c}_k = \mathbf{h}(k)$
  - 6: **for** Number of iterations **do**
  - 7:   **for**  $k = 1, \dots, K$  **do**
  - 8:     Find set  $S_k$  of  $g$  with  $|h(g)\mathbf{c}_k| = \max_{\hat{k}} |\mathbf{H}\mathbf{c}_{\hat{k}}|$
  - 9:      $\mathbf{c}_k = \frac{\sum_{S_k} h(g)}{|\sum_{S_k} h(g)|}$
  - 10:   **end for**
  - 11: **end for**
- 

---

#### Algorithm 2 $k$ -means PO Algorithm

---

- 1:  $M$  number of measurements
  - 2:  $k = 1, \dots, K; \mathbf{C} \in \mathbb{C}(N_{\text{antennas}} \times K) = \mathbf{c}_1, \dots, \mathbf{c}_K$
  - 3:  $\mathbf{H} \in \mathbb{C}(M \times N_{\text{antennas}})$
  - 4: Randomly choose  $K$  different indices of measurements
  - 5: Define center of cluster as  $\mathbf{c}_k = e^{j\arg(\mathbf{h}(k))}$
  - 6: **for** Number of iterations **do**
  - 7:   **for**  $k = 1, \dots, K$  **do**
  - 8:     Find set  $S_k$  of  $g$  with  $|h(g)\mathbf{c}_k| = \max_{\hat{k}} |\mathbf{H}\mathbf{c}_{\hat{k}}|$
  - 9:      $\mathbf{c}_k = \frac{\sum_{S_k} e^{j\arg(h(g))}}{\sum_{S_k} 1}$
  - 10:   **end for**
  - 11: **end for**
- 

### B. Results

Fig. 11 shows exemplary the clustering results for the  $k$ -means MRT-based clustering algorithm for  $k = 40$  clusters after 30 iterations. The positions of the specific channel measurement are colored according to their respective cluster. Fig. 12 shows the clustering results for the  $k$ -means PO clustering algorithm for the respective value of  $k$ , number of iterations and the same randomly picked initial cluster centers. Obviously, channel measurements which are locally close to each other are grouped into the same cluster. The result shows an expected behavior from other channel models. It is yet another sanity check for the measurements. The regions with low SNR result in higher diversity of clusters (with, yet, only small contribution to sum rate) and the regions with higher SNRs show more separated clusters. The reason for this effect is that two channels “decorrelate” with increasing noise power.

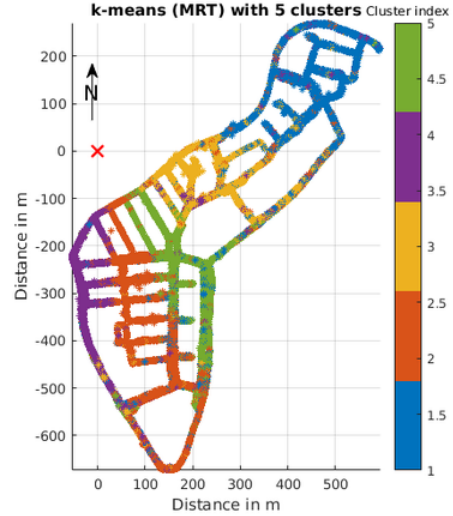


Fig. 9: Result of a  $k = 5$  means MRT clustering



Fig. 10: Result of a  $k = 5$  means PO clustering

To evaluate the results of the clustering algorithms, the sum-rate was calculated while assuming an interference-limited channel. To account for the noise, the signal-to-interference ratio (SIR) is clipped to a SIR of 30 dB.

The  $\text{SIR}_u$  for user  $u$  that belongs to cluster  $k$  is calculated according to

$$\text{SIR}_u = \frac{|\mathbf{h}_u \mathbf{c}_k|^2}{\sum_{\hat{k} \neq k} |\mathbf{h}_u \mathbf{c}_{\hat{k}}|^2}. \quad (2)$$

The cluster  $\text{SIR}_k$  is calculated by the median of the  $\text{SIR}_u$  of all users within this cluster  $k$ . The interference is calculated by the sum of the energy for user  $u$  from all clusters  $\hat{k}$  without cluster  $k$ .

$$\text{SIR}_k = \text{median}(\text{SIR}_u) \text{ with } \forall u \in \text{cluster } k \quad (3)$$

The sum-rate  $R_{\text{sum}}$  is calculated by the sum of the rate of its respective cluster  $\text{SIR}_k$ .



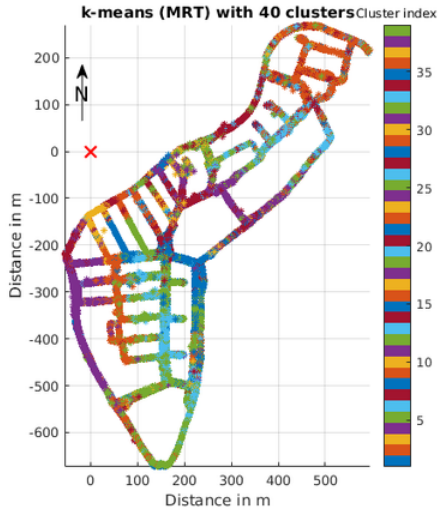


Fig. 11: Result of a  $k = 40$  means MRT clustering

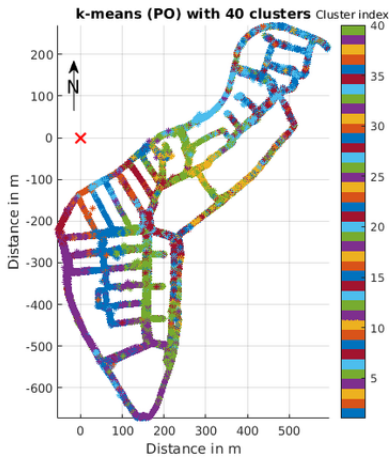


Fig. 12: Result of a  $k = 40$  means PO clustering

$$R_{\text{sum}} = \sum_k \log_2(1 + \text{SIR}_k) \quad (4)$$

Fig. 13 shows the mean of the sum-rate after 1000 random initializations of the  $k$ -means clustering algorithm. The increasing number of clusters results in a small increase of the sum-rate. After  $k \geq 20$  clusters, MRT-precoding begins to significantly outperform PO-precoding. Note that MRT-precoding should be better than PO-precoding for all  $k$ , indicating that the number of random initializations for computing the median could still be increased.

However, the result also indicates that the lower complexity PO-precoding only incurs a small loss with respect to MRT-precoding for lower number  $k$  of clusters. For a small number of clusters, e.g.,  $k = 5$ , both clustering algorithms converge to nearly the same clusters. For small  $k$ , e.g.,  $k < 20$ , the PO-algorithm approaches the MRT-algorithm performance very closely. Note that, the PO-algorithm considers only the phase

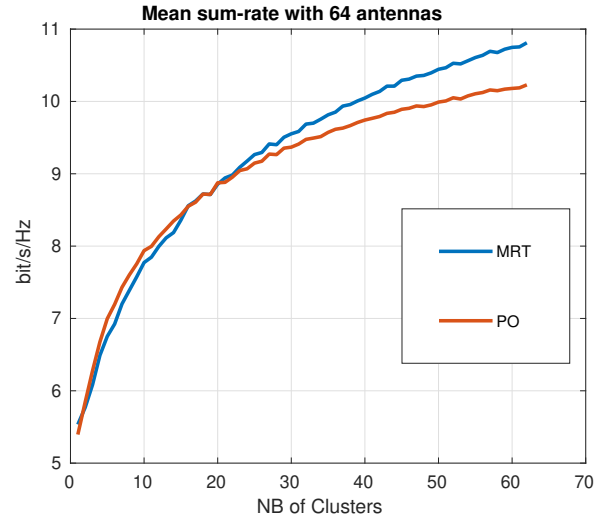


Fig. 13: Mean sum-rate versus number of clusters  $k$  (64 antennas) averaged over 1000 cluster realizations on the measured data

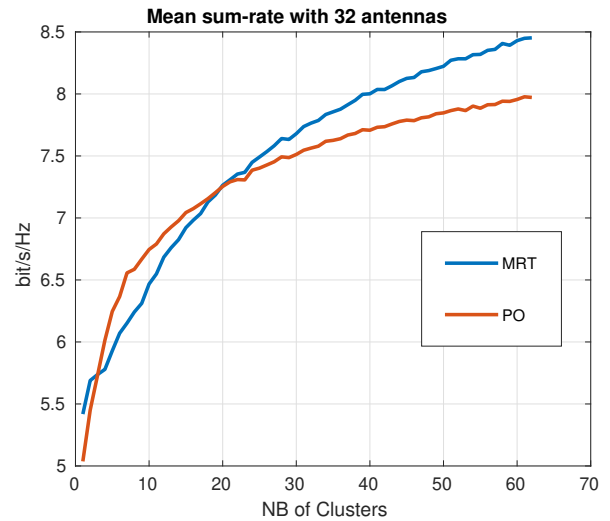


Fig. 14: Mean sum-rate versus number of clusters  $k$  (32 antennas) averaged over 1000 cluster realizations on the measured data

and is, thus, of much lower complexity (akin beam-forming). The beam-forming characteristics can clearly be observed in Fig. 10 and Fig. 9. If the number of clusters  $k$  increases to, e.g.,  $k = 40$ , the clusters have to be separated not only in the angular direction but also in the radial distance, such that several clusters are “behind” each other in radial direction; in this case, the MRT-algorithm outperforms the PO-based cluster algorithm. Fig. 11 and Fig. 12 show the different clustering results for the exact same initial cluster centers for  $k = 40$ .

#### IV. CONCLUSIONS

In this paper, we presented massive MIMO channel measurements, collecting a large quantity of channel state information over a wide residential area. The  $k$ -means clustering algorithm was applied to this CSI-data by using MRT and PO-precoding, respectively. As one interesting result, PO-precoding, which is of much lower complexity, turns out to lose only little in terms of sum-rate when compared to the full MRT-precoding.

#### REFERENCES

- [1] E. Björnson, J. Hoydis and L. Sanguinetti, *Massive MIMO Networks: Spectral, Energy, and Hardware Efficiency*. Now Publisher, Feb. 2017.
- [2] E. G. Larsson, O. Edfors, F. Tufvesson, and T. L. Marzetta, "Massive MIMO for next generation wireless systems," *IEEE Communications Magazine*, 2014.
- [3] J. Hoydis, S. ten Brink, and M. Debbah, "Massive MIMO in the UL/DL of Cellular Networks: How Many Antennas Do We Need?" *IEEE Journal on Selected Areas in Communications*, 2013.
- [4] S. Jaeckel, L. Raschkowski, K. Borner, and L. Thiele, "QuaDRiGa: A 3-D multi-cell channel model with time evolution for enabling virtual field trials," *IEEE Trans. Antennas Propag.*, pp. 1–6, Oct. 2014.
- [5] R. S. Ganesan and W. Zirwas and B. Panzner and K. I. Pedersen and K. Valkealahti, "Integrating 3D Channel Model and Grid of Beams for 5G mMIMO System Level Simulations," in *Vehicular Technology Conference*, Sept. 2016, pp. 1–6.
- [6] USRP User Manual, Ettus Research. [Online]. Available: <https://www.ettus.com/>
- [7] T. Takasu and A. Yasuda, "Development of the low-cost RTK-GPS receiver with an open source program package RTKLIB," International Symposium on GPS/GNSS, International Convention Center Jeju, Korea, November 4-6, Tech. Rep., 2009.
- [8] M. Arnold and J. Hoydis and S. ten Brink, "Novel Massive MIMO Channel Sounding Data Applied to Deep Learning-based Indoor Positioning," *International Conference on Systems, Communications and Coding (SCC)*, pp. 1–6, Feb. 2019.
- [9] M. Arnold, J. Pfeiffer, and S. ten Brink, "Area Rate Evaluation based on Spatial Clustering of massive MIMO Channel Measurements," in *WSA 2018; 22nd International ITG Workshop on Smart Antennas*, March 2018, pp. 1–6.